

---

# Unfolding Generative Flows with Koopman Operators: Fast and Interpretable Sampling

---

**Erkan Turan**

LIX, École Polytechnique, IP Paris

**Aristotelis Siozopoulos**

LIX, École Polytechnique, IP Paris

**Maks Ovsjanikov**

LIX, École Polytechnique, IP Paris

## Abstract

Conditional Flow Matching (CFM) offers a simulation-free framework for training continuous-time generative models, bridging diffusion and flow-based approaches. However, sampling from CFM still relies on numerically solving non-linear ODEs which can be computationally expensive and difficult to interpret. Recent alternatives address sampling speed via trajectory straightening, mini-batch coupling or distillation. However, these methods typically do not shed light on the underlying *structure* of the generative process. In this work, we propose to accelerate CFM and introduce an interpretable representation of its dynamics by integrating Koopman operator theory, which models non-linear flows as linear evolution in a learned space of observables. We introduce a decoder-free Koopman-CFM architecture that learns an embedding where the generative dynamics become linear, enabling closed-form, one-step sampling via matrix exponentiation. This results in significant speedups over traditional CFM as demonstrated on controlled 2D datasets and real-world benchmarks, MNIST, Fashion-MNIST (F-MNIST), and the Toronto Face Dataset (TFD). Unlike previous methods, our approach leads to a well-structured Koopman generator, whose spectral properties, eigenvalues, and eigenfunctions offer principled tools for analyzing generative behavior such as temporal scaling, mode stability, and decomposition in Koopman latent space. By combining sampling efficiency with analytical structure, Koopman-enhanced flow matching offers a potential step toward fast and interpretable generative modeling. Code available [here](#).

## 1 Introduction

Generative models based on continuous-time dynamics have made significant progress in recent years, particularly through the lens of diffusion models, flow matching and related methods [7, 4, 36, 22]. These frameworks define a transformation from a simple prior distribution to a complex data distribution via an ordinary differential equation (ODE), where the learned velocity field governs the generative process. Conditional Flow Matching (CFM) [45, 46] is a unifying and simulation-free approach, which learns this velocity field without requiring numerical simulations during training. While CFM accelerates training and offers a principled framework, test-time sampling remains a challenge due to the computational cost of numerically integrating nonlinear trajectories.

A major bottleneck in such generative pipelines lies in the non-linear nature of the learned flows, where the curvature and stiffness of the vector fields require fine-grained integration schemes for accurate generation. To reduce this burden, a range of techniques have recently been proposed, including flow straightening, minibatch couplings, and distillation-based methods [45, 37, 11] among

many others. However, existing approaches still operate within inherently non-linear regimes, limiting both sampling efficiency and interpretability.

In this paper, we explore an alternative route by leveraging Koopman operator theory [19, 5], a classical tool from dynamical systems that linearizes nonlinear evolution in a lifted function space. By representing the state evolution in terms of observable functions, the Koopman framework transforms nonlinear dynamics into linear ones, enabling analytical propagation of trajectories and enabling interpretability via spectral analysis [39, 29]. We propose a decoder-free approach for learning Koopman embeddings of the CFM vector fields, enabling fast sampling via matrix exponentiation and simplifying the inference pipeline. Our contributions are as follows:

- We introduce a Koopman-theoretic formulation of Conditional Flow Matching, casting the nonlinear learned dynamics into a linear operator framework.
- We develop a decoder-free learning architecture that stabilizes training and facilitates analytical sampling.
- We empirically demonstrate competitive performance and superior sampling speed across several benchmarks, with added interpretability via spectral decomposition.

## 2 Related Work

Our work builds upon two primary research directions: the Koopman operator theory for dynamical systems and flow-based generative models, particularly Conditional Flow Matching (CFM). Below, we focus on the most closely related approaches. We also touch upon existing efforts to bridge operator-theoretic approaches with generative modeling.

### 2.1 Koopman Operator Theory

Koopman Operator Theory provides a powerful framework for representing and analyzing nonlinear dynamical systems [19, 20, 6, 49, 5, 3]. Instead of studying the evolution of states in a nonlinear state space, the Koopman operator describes the evolution of observable *functions* of the state. This evolution is linear, albeit in an infinite-dimensional embedding space, enabling the application of linear systems theory to complex nonlinear dynamics. Recent advancements have focused on leveraging learning-based techniques, such as Dynamic Mode Decomposition (DMD) and its variants [21], as well as neural network-based approaches like Koopman autoencoders [28, 32, 1], to learn finite-dimensional approximations of the Koopman operator from trajectory data. These methods have been applied in a range of fields, including fluid dynamics [39], power systems [44], and molecular dynamics [18], among others. The focus has largely been on system identification, prediction, and control. Some works have explored the Koopman operator for understanding the evolution of probability densities [30, 39], which is closely related to our interpretability analysis.

### 2.2 Flow-Based Generative Models and Conditional Flow Matching

Generative modeling has seen remarkable progress, with flow-based models emerging as a prominent class offering tractable likelihoods and exact sampling [9, 10, 17, 40, 41, 15, 48]. These models learn an invertible mapping from a simple base distribution (e.g., a Gaussian) to some given data distribution. Continuous Normalizing Flows (CNFs) [8] parameterize this mapping as the solution to an ordinary differential equation (ODE), viewing the generation process as a continuous transformation.

Conditional Flow Matching (CFM) [22, 45, 26] represents a significant advancement in training CNFs. CFM methods typically define a probability path (often a simple interpolation or a Gaussian conditional path) between pairs of source (e.g., noise) and target (e.g., data) samples, and then train a neural network to approximate the time-dependent vector field that gives rise to these paths. This approach offers simulation-free training, improved stability, and often better performance compared to earlier CNF training techniques. CFM has been successfully applied to various generative tasks, including image generation, single-cell dynamics, unsupervised image translation [22, 46] and molecule generation [16] among many others. Variants like Optimal Transport CFM (OT-CFM) aims to learn more direct and potentially “straighter” transformations from noise to data [45, 37], which improves sampling.

### 2.3 Efficient and One-Step Sampling

The non-linear nature of CFM and the need to integrate the learned vector field at test time has motivated extensive work on more efficient sampling strategies. Building on regularization strategies such as (OT-CFM) [22, 45, 37], recent advancements including consistency models [42], latent consistency models [27], and rectified flows [25] have helped to drastically reduce the number of sampling steps, often achieving high-quality generation in very few steps, or even a single step [11, 23]. Our work highlights the potential for Koopman operator theory to contribute to the design or understanding of such efficient sampling trajectories within CFM-like frameworks.

Concurrent to our work, Berman et al. [2] propose a Koopman-based generative model by learning a discrete-time Koopman operator that directly maps between noisy samples at  $t = 0$  and target data at  $t = 1$ . While their approach is primarily positioned as an enhancement to diffusion models, although not exclusive to it, *our work focuses on conditional flow matching*, framing the problem as supervised learning of vector fields over time. In contrast to their discrete formulation, *we explicitly model the full continuous-time dynamics* by learning the *Koopman generator*, providing access to the entire latent flow from  $t = 0$  to  $t = 1$ . This not only preserves interpretability of the intermediate dynamics but also aligns naturally with the flow matching paradigm.

## 3 Background and Motivation

Our main goal is to bridge the gap between Conditional Flow Matching (CFM) approaches and Koopman Operator Theory. At a high level, the Koopman framework allows one to represent any non-linear dynamical system as a linear system in a high (possibly infinite) dimensional space. The major challenges associated with applying this formalism to CFM are as follows:

1. The standard approach for Koopman operator learning assumes autonomous (time-independent) dynamics, whereas CFM is inherently a time-dependent process.
2. Learning Koopman auto-encoders relies on *decoding* from a high-dimensional latent space, which can be error-prone and unstable.
3. CFM is formulated in terms of the underlying vector fields that capture infinitesimal changes, whereas Koopman operators typically consider the dynamics themselves.

Below we introduce a framework that addresses all of these issues and presents the first direct and learnable representation of Conditional Flow Matching via Koopman operator theory.

For completeness, we review the key concepts below, before describing our computational approach.

### 3.1 Conditional Flow Matching

Conditional Flow Matching (CFM) is a simulation-free learning objective for training continuous-time generative models. The main objective of CFM is to learn a velocity field  $v_t(x)$  that transports a simple prior distribution  $x_0 \sim \pi$  to the data distribution  $x_1 \sim q_1$  via the flow induced by an ordinary differential equation (ODE):

$$\frac{d\phi_t(x)}{dt} = v_t(\phi_t(x)), \quad (1)$$

where  $\phi_t$  denotes the flow map which can be simply interpreted as a smooth time-continuous change of variables. These induced paths are naturally associated with a path probability density  $p_t(x)$  which evolves according to the continuity equation, expressing the conservation of probability mass:

$$\frac{\partial p_t}{\partial t} = -\nabla \cdot (v_t(x)p_t(x)), \quad (2)$$

Training this model requires learning the vector field, which can be parameterized by a neural network  $v_\theta(x, t)$ . One naive training objective could be to regress the parameterized vector field to the underlying ground-truth vector field:

$$\mathcal{L}_{\text{FM}}(\theta) = \mathbb{E}_{t, x_0, x_t} \|v_\theta^\theta(x_t) - v_t(x_t)\|^2, \quad (3)$$

However, this objective poses two obstacles 1) During training, we do not have access to the vector field  $v_t$ . 2) We cannot efficiently sample  $x_t$ . Lipman et al. [22] observe that marginalizing the path probability density leads to:

$$p_t(x) = \int p_t(x|x_1)q(x_1)dx_1 \quad (4)$$

where  $q(x_1)$  is the data distribution and  $p_t(x|x_1)$  denotes a hand-designed conditional path distribution, constrained to yield trajectories that terminate at the prescribed target  $x_1$ . This distribution needs to satisfy two conditions:  $p_1(x|x_1) \approx x_1$  and  $p_0(x|x_1) \approx \pi$  where  $\pi$  is the prior distribution. To achieve this, the authors of [22] introduce two kernels: a Gaussian path and an OT-based path. The conditional probability in Eq. (4) also obeys a continuity equation that is induced by a *conditional* vector field  $u_t(x|x_1)$ . In their work, they show that with  $p_t(x|x_1)$  and  $u_t(x|x_1)$  we can reconstruct the full vector field and can derive a tractable simulation-free training objective:

$$\mathcal{L}_{\text{CFM}}(\theta) = \mathbb{E}_{x_0, x_t, x_1, t} \|v_t^\theta(x_t) - u_t(x|x_1)\|^2. \quad (5)$$

As they show, this leads to the same optimization solution as the original loss in Eq.(3) since  $\nabla_\theta \mathcal{L}_{\text{FM}} = \nabla_\theta \mathcal{L}_{\text{CFM}}$ .

Although CFM eliminates simulation-based training, sampling still requires numerically integrating the learned ODE. The number of integration steps needed for accurate generation is related to the curvature of the trajectories: a higher curvature demands more precise (and expensive) solvers. Existing approaches to reduce sampling cost include straightening the learned trajectories via optimal transport, using rectified flows, or distilling the model into shallower networks. However, these solutions typically preserve non-linearity in the dynamics, making interpretability and global analysis difficult [45, 37, 11]. In contrast, we aim to globally linearize the system via Koopman theory, which allows faster sampling with additional analysis tools from spectral theory.

### 3.2 Koopman Operator Theory

As mentioned above, Koopman operator theory offers a classical dynamical systems perspective for linearizing non-linear systems [19, 5]. Rather than acting on the state space directly, the Koopman operator advances measurement *functions* of the state of the dynamical system via composition with the system’s flow map.

Consider a finite-dimensional state space  $\mathcal{X} \subseteq \mathbb{R}^n$ , which could correspond, e.g., to the image state space  $\mathbb{R}^{d \times d}$  with  $d$  the number of pixels. Suppose that  $\mathcal{X}$  is undergoing dynamics driven by  $v(x)$  (notice that the dynamics are *time-independent*). Such dynamics on the state space induce a discrete flow-map  $F_{\Delta t} : \mathcal{X} \rightarrow \mathcal{X}$  defined as:

$$F_{\Delta t}(x_t) = x_t + \int_t^{t+\Delta t} v(x_\tau) d\tau = x_{t+\Delta t}. \quad (6)$$

Instead of acting on the state-space  $\mathcal{X}$ , the key idea behind the Koopman operator is to consider the space of *measurement functions* of the states  $\mathcal{G}(\mathcal{X})$ , which can be, e.g., the  $L^2(\mathcal{X})$  Hilbert space of square-integrable functions. On such a space we can define the discrete Koopman operator  $\mathcal{K}_{\Delta t}$

$$\mathcal{K}_{\Delta t}g(x_t) := (g \circ F_{\Delta t})(x_t) = g(F_{\Delta t}(x_t)) = g(x_{t+\Delta t}). \quad (7)$$

Defined as such, the operator is trivially linear (regardless of the non-linearity of  $F_{\Delta t}$ ) due to the linearity of the composition of the function indeed:  $\mathcal{K}_{\Delta t}(g_1 + g_2)(x) = (g_1 + g_2) \circ F_{\Delta t}(x) = g_1 \circ F_{\Delta t}(x) + g_2 \circ F_{\Delta t}(x) = \mathcal{K}_{\Delta t}g_1(x) + \mathcal{K}_{\Delta t}g_2(x)$ .

In essence, the Koopman formalism enables the transformation of finite-dimensional nonlinear dynamics into linear dynamics in a (potentially infinite-dimensional) functional space, regardless of the nonlinearity of the underlying system. This perspective is illustrated in Figure 1 (right), where the evolution of the system is recast as linear operator dynamics on a lifted representation. This idea is reminiscent of Functional Maps [33] used in shape processing, but here extended with an explicit temporal (dynamical) component.

The *continuous-time* analogue of Eq. (7) is given by the *Koopman generator*, or Lie operator [5]:

$$\mathcal{L}g(x_t) = \lim_{\Delta t \rightarrow 0} \frac{\mathcal{K}_{\Delta t}g(x_t) - g(x_t)}{\Delta t} = \frac{dg(x_t)}{dt} = \nabla_x g(x_t) \cdot v(x_t), \quad (8)$$



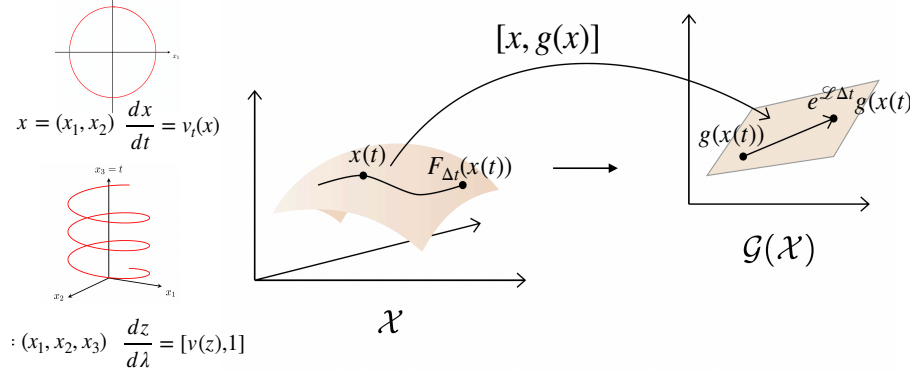


Figure 1: **Conceptual illustration of Koopman operator theory.** Left: Transforming non-autonomous dynamics in state-space into autonomous dynamics in a time-augmented state-space. Right: A non-linear dynamical system in state space  $\mathcal{X}$  with complex trajectories. The same system transformed into a linear evolution in the lifted space of observables  $\mathcal{G}(\mathcal{X})$ , where future states can be predicted via matrix exponentiation  $e^{\mathcal{L}\Delta t}$

which describes the infinitesimal evolution of observables under the vector field  $v(x)$ . It is also linear and is related to  $\mathcal{K}$  by  $\mathcal{K}_{\Delta t} = e^{\mathcal{L}\Delta t}$ .

Koopman’s theory typically leads to infinite-dimensional representations, but if one can find a finite set of eigenfunctions  $\{g_i\}_{i \in [1, p]}$  such that:

$$\mathcal{L}g_i = \lambda_i g_i, \quad (9)$$

then we can define a *stable subspace* of the state-measurement functions  $\mathcal{G}(\mathcal{X})$ . Indeed the span of these eigenfunctions is stable under the action of the Lie operator, i.e.:

$$\mathcal{L} \sum_i \alpha_i g_i = \sum_i \alpha_i \mathcal{L}g_i = \sum_i \alpha_i \lambda_i g_i \subseteq \text{Span}(g_1, \dots, g_p) \quad (10)$$

The Lie operator can therefore be approximated by its restriction to this eigenspace via  $\mathbf{L} = \mathcal{L}|_{\text{Span}(g_i)}$ . This is a finite-dimensional approximation of the full linear operator which can take a convenient matrix form acting on  $\mathbb{R}^p$  with the coordinates given by the values of  $g_i$ . Stacking the eigenfunctions, this implies that the evolution in the lifted space can be written as:

$$\frac{d}{dt} \begin{bmatrix} g_1(x_t) \\ \vdots \\ g_p(x_t) \end{bmatrix} = \mathbf{L} \begin{bmatrix} g_1(x_t) \\ \vdots \\ g_p(x_t) \end{bmatrix}. \quad (11)$$

where bold symbols denote vector and matrix quantities. Note that if  $g_i$  forms an eigenspace then  $\mathbf{L}$  is a diagonal matrix of eigenvalues. More broadly,  $\mathbf{L}$  is a general dense matrix if  $g_i$  represents a set that simply forms an invariant subspace. In either case, this is a linear system that can be solved by matrix exponentiation or diagonalization:

$$\mathbf{g}(x_t) = e^{t\mathbf{L}}\mathbf{g}(x_0). \quad (12)$$

In this work, we propose to leverage this structure to represent the dynamics in Conditional Flow Matching. By learning an encoding of the state into such a Koopman-invariant space, we transform the sampling problem into one of matrix exponentiation and multiplication which is parallelizable and efficient. Furthermore, we leverage this formalism to shed light on the information contained in the spectrum of the Koopman operator. As we demonstrate below, this provides insights into the structure and stability of the learned generative process.

## 4 Method

Our main objective is to represent Conditional Flow Matching (CFM) by lifting the non-linear learned dynamics into a space where they evolve linearly. To do so, we leverage Koopman operator theory

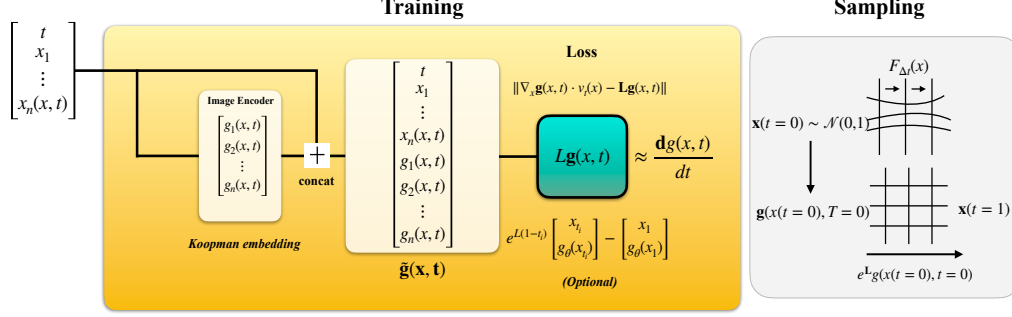


Figure 2: **Overview of the Koopman-CFM framework.** Left: Training pipeline showing the encoder architecture that maps state-time pairs to the Koopman embedding space where dynamics are linear. The training objective enforces consistency between the Koopman generator and the learned CFM vector field. Right: Sampling procedure showing how one-step generation is achieved through matrix exponentiation

described above and introduce a simple decoder-free approach to learning this linear embedding. Our method enables efficient “one-shot” sampling and offers spectral insight into the learned dynamics.

#### 4.1 Lifting CFM with Koopman Theory

In standard CFM, we learn non-autonomous dynamics of the form of Eq. (1), where, contrary to the standard Koopman setting, the velocity field  $v_t$  depends explicitly on time. To apply Koopman theory, which is classically defined for autonomous systems, we augment the state with time [43],  $x_t \mapsto (y, x_t)$ , where  $y = t$ , and reformulate the dynamics accordingly:  $v_t(x) \mapsto \left(\frac{dy}{dt}, \frac{dx_t}{dt}\right) = (1, v_y(x))$ , yielding a time-independent vector field  $v(y, x) = (1, v_y(x))$ . In this lifted formulation, time is treated as an additional state variable, effectively embedding the temporal dependence into an augmented autonomous system. This approach is illustrated on the left side of Figure 1, where the time-augmented state enables Koopman operator theory to be applied with minor modifications.

#### 4.2 Decoder-Free Koopman Learning

Previous efforts for learning the Koopman embedding focused primarily on an encoder-decoder approach [28, 32, 1], which learns an embedding into a higher-dimensional space. In our experiments, we observed that training a decoder can be unstable and error-prone, even for relatively simple dynamics. Instead, we make the following observation: if  $x \in \mathbb{R}^n$  then the identity mapping  $\text{id}(x) = x$  can be considered as  $n$  projection functions. I.e.,  $f^j(x) = x^j$ , where  $x^j$  is the  $j^{\text{th}}$  coordinate of  $x$ . Moreover, each of these  $f_j$  can be considered to be an observable, which should evolve linearly in function space:

$$\mathcal{K}_{\Delta t} f_j(x_t) = f_j \circ F_{\Delta t}(x_t) = x_{t+\Delta t}^j. \quad (13)$$

This motivates the decision of discarding the decoder and parameterizing the encoder as follows:

$$\tilde{g}(x) = [x, g_\theta(x)]. \quad (14)$$

In other words, we concatenate the state itself to the learned non-linear measurements. This design choice, as illustrated in Figure 2 avoids the instability of training and reduces the error coming from the potential suboptimality of the decoder. It also simplifies inference and in practice significantly helps to obtain accurate sampling capabilities as seen in 5.1. A byproduct of this parametrization is a natural spectral visualization tool, as we mention in Section 5.2.

#### 4.3 Koopman Encoder Training

To train the Koopman encoder, we first enforce the consistency between the Koopman generator and the underlying velocity field.

---

**Algorithm 1** Training Procedure

---

**Require:** Fixed pre-trained vector fields  $v_t$ , CFM-generated trajectories  $\text{traj}$ , trainable encoder  $g_\theta(x, t)$ , trainable Koopman generator  $\mathbf{L}_\varphi$

- 1: **for** each training step **do**
- 2:   Sample batch  $(x_t, t), x_1 \in \text{traj}$
- 3:   Encode:  $\mathbf{z}_t \leftarrow \tilde{g}_\theta(x_t, t), \mathbf{z}_1 \leftarrow \tilde{g}_\theta(x_1, 1)$
- 4:   Compute  $\mathcal{L}_{\text{generator}}(x_t) \leftarrow \|\mathbf{L}_\varphi \mathbf{z}_t - \nabla_x \mathbf{z}_t \cdot \mathbf{v}_t(x)\|^2$
- 5:   (Optional)  $\mathcal{L}_{\text{consistency}}(x_t) \leftarrow \|e^{\mathbf{L}_\varphi(1-t)} \mathbf{z}_t - \mathbf{z}_1\|^2$
- 6:   (Optional)  $\mathcal{L}_{\text{prediction}}(x_t) \leftarrow \|\text{Proj}(\mathbf{L}_\varphi \mathbf{z}_t) - \mathbf{v}_t(x)\|^2$
- 7:   Update  $\tilde{g}_\theta, \mathbf{L}_\varphi$  via backprop
- 8: **end for**

---



---

**Algorithm 2** Sampling Procedure

---

**Require:** Sampling time  $t$ , encoder  $g_\theta(x, t)$ , generator  $\mathbf{L}$

- 1: Sample  $x_0 \sim \mathcal{N}(0, 1)$
- 2: Encode:  $\mathbf{z}_0 \leftarrow \tilde{g}_\theta(x_0, 0)$
- 3: Evolve:  $\mathbf{z}_t \leftarrow e^{\mathbf{L}t} \mathbf{z}_0$
- 4: Decode:  $x_t \leftarrow \text{Proj}(\mathbf{z}_t)$

---

Figure 3: Side-by-side presentation of (left) training and (right) sampling procedures for Koopman-CFM.

#### Generator loss (Koopman consistency):

$$\mathcal{L}_{\text{gen}} = \mathbb{E}_{t, x_t} \|\mathbf{L} \tilde{g}_\theta(x_t) - \nabla \tilde{g}_\theta(x_t) \cdot \mathbf{v}_y(x_t)\|^2, \quad (15)$$

Where  $\mathbf{v}_y$  is a fixed pre-trained CFM model that serves as a target time-independent velocity field. An additional loss term stated in Eq. (16) below that we found beneficial (see Table 2 in Supplementary) is the **target consistency objective**. This loss encourages agreement between the Koopman-evolved representation from an intermediate time point  $t_i \in [0, 1)$  and the final generated state at  $t = 1$ . Specifically, we measure how well the Koopman operator, applied from  $t_i$  to  $t = 1$ , can predict the full state-observable embedding at the final time:

#### (Optional) Target consistency loss:

$$\mathcal{L}_{\text{target}} = \mathbb{E}_{t_i, x_{t_i}} \left\| e^{\mathbf{L}(1-t_i)} \begin{bmatrix} x_{t_i} \\ g_\theta(x_{t_i}) \end{bmatrix} - \begin{bmatrix} x_1 \\ g_\theta(x_1) \end{bmatrix} \right\|^2. \quad (16)$$

For computational efficiency, we evaluate this loss on batches of samples taken at the same  $t_i$ , allowing the matrix exponential  $e^{\mathbf{L}(1-t_i)}$  to be shared across the batch. Inspired by curriculum learning, we progressively decrease  $t_i$  from 1 to 0 during training, under the intuition that short-term predictions are easier to learn initially and help to stabilize learning for longer time horizons.

## 4.4 Koopman-Based Sampling and Spectral Analysis

Once the encoder and Koopman operator  $\mathbf{L}$  are learned, sampling reduces to closed-form evolution: given an initial encoded state  $\tilde{\mathbf{g}}(x_0)$ , we compute  $\tilde{\mathbf{g}}(x_t) = e^{\mathbf{L}t} \tilde{\mathbf{g}}(x_0)$ . If  $\mathbf{L}$  is diagonalizable with  $\mathbf{L} = \mathbf{P} \mathbf{\Lambda} \mathbf{P}^{-1}$ , this can be efficiently evaluated via matrix exponentiation. Final samples are obtained by projecting back to the original state space using the identity component of the observable.

Beyond efficient sampling, the linear structure of  $\mathbf{L}$  provides valuable insights into the dynamics. Its eigenvectors define spatially coherent modes, while the real parts of the eigenvalues,  $\text{Re}(\lambda_i)$ , indicate the stability and temporal scales of these modes—decay for  $\text{Re}(\lambda_i) < 0$  and growth for  $\text{Re}(\lambda_i) > 0$ . Our decoder-free architecture allows direct visualization of eigenfunctions via:

$$\mathbf{x} = \text{Proj}_{\text{state}}(\tilde{\mathbf{g}}_i(x)). \quad (17)$$

Sorting eigenvalues by their real part reveals the dominant modes governing the generative process, as further demonstrated in our experiments. Training and sampling are performed via the algorithms 3.

## 5 Experimental results and discussion

### 5.1 2D Toy Experiments

We validate our approach on standard 2D generative benchmarks: **Eight Gaussians**, **Two Moons**, and **Swiss Roll**. These datasets are commonly used to assess the quality of learned generative flows due to their nonlinear structure and visual interpretability. **Eight Gaussians** is a mixture model with eight modes arranged in a circle, testing mode coverage and stability. The **Two Moons** dataset consists of two interleaving half-circles in 2D space. **Swiss Roll** contains a 2D manifold embedded in 3D, resembling a rolled ribbon. Both the **Two Moons** and the **Swiss Roll** datasets are readily available in the Scikit-Learn library [35]. We first learn the vector fields generating these datasets using the CFM pipeline and then fix its parameters for subsequent analysis. These low-dimensional settings allow for direct visualization of both the learned trajectories and the Koopman measurement functions.

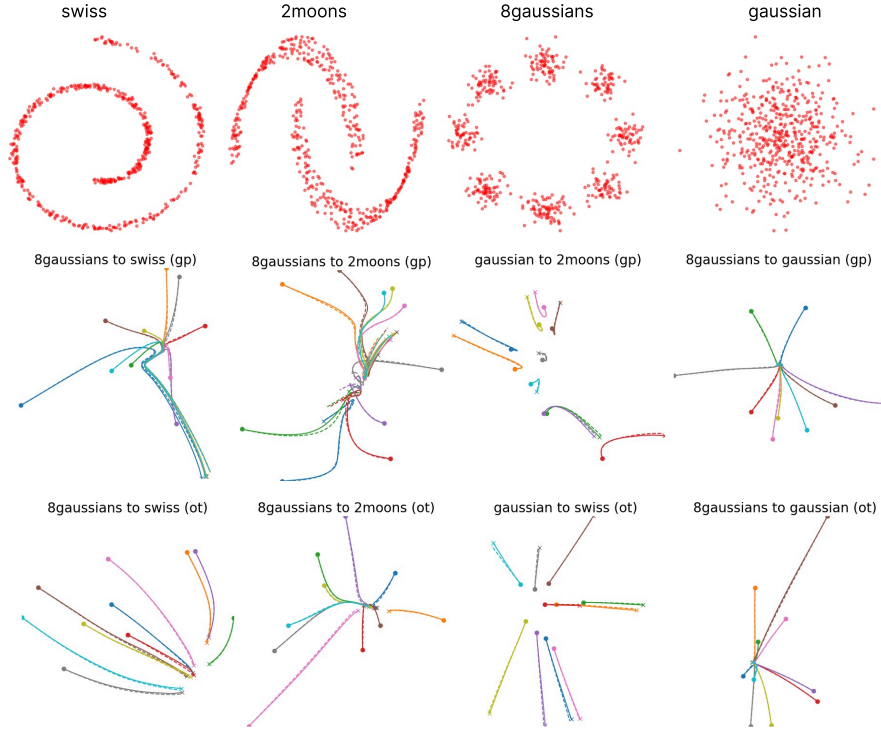


Figure 4: Trajectory comparisons between CFM and Koopman-CFM across 2D datasets using Gaussian and OT interpolation paths. **Top row**: datasets utilized. **Middle row**: the Koopman-predicted rollouts (dashed lines) vs CFM dynamics (solid line) for Gaussian-Paths. **Bottom row**: comparison for OT-Paths. In both cases the Koopman trajectories align closely with CFM dynamics (solid lines), and we see that our method correctly incorporates the time dependency throughout the temporal domain regardless of path curvature.

To test our method, we represent the Koopman operator as an unconstrained matrix and parameterize  $g_\theta(x)$  using a 10-layer MLP with 200 hidden units and SiLU activations (shallower architectures also perform well; see Appendix). Training spans  $x \in [-8, 8]^2$  across  $t \in [0, 1]$ , following our generator consistency and target alignment objectives. Figure 4, shows the 2D datasets utilized and compares the trajectories of the underlying CFM dynamics and the Koopman predicted rollouts for selected highly non-linear dynamics. Figure 2 in the Supplementary compares the predicted trajectories from Koopman-CFM and the original CFM model across all datasets and path types (OT and Gaussian interpolation) showing the robustness of our model upon these two factors. Koopman-

CFM accurately reproduces both straight and curved paths across the full-time domain at a fraction of the original sampling time. The decoder-free architecture, discarding error coming from a non-optimal decoder is essential to achieve this level of trajectory accuracy as seen in Section B.2 in the Supplementary Material. The initial points are taken randomly over the 2D domain and consistently yield accurate results illustrating the ability to generalize beyond local training points. This shows that our parametrization allows us to obtain an accurate Koopman representation even for the time-dependent dynamics of CFM. Indeed, figure 5 shows the vector field learned by Koopman-CFM at different time steps on the SWISS ROLL dataset under OT path dynamics. The model successfully captures the curved transport structure and its time evolution, validating our time-augmentation approach for handling non-autonomous systems.

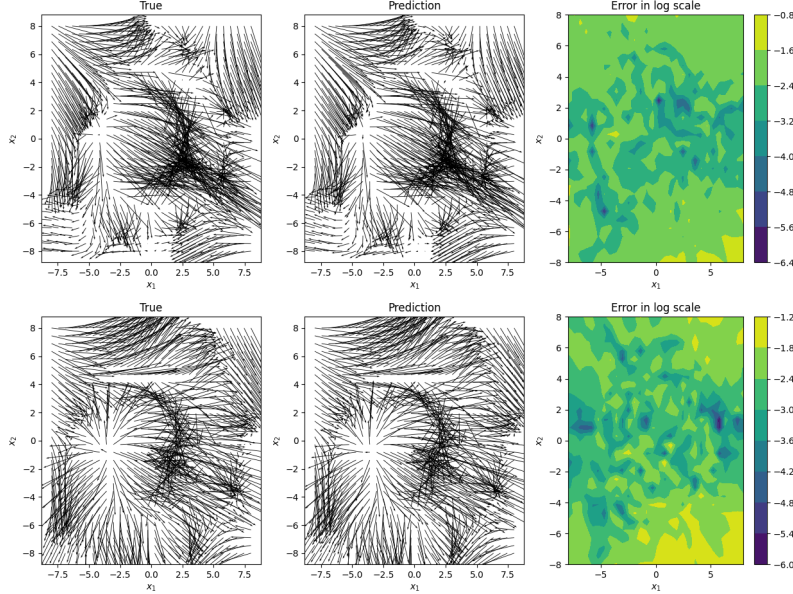


Figure 5: Learned vector fields at different time steps for the Swiss Roll dataset under OT path dynamics, starting from an 8-Gaussian prior. Left column: True vector field. Center column: Koopman predicted vector field, Right: Error in log scale between Koopman and true vector field. The rows correspond to different times  $t$ . We see that augmenting the state with time enables Koopman-CFM to approximate non-autonomous dynamics effectively and linearly in the lifted space.

To quantitatively validate these claims, we also report full Maximum-Mean-Discrepancy (MMD) scores [13]—a kernel-based statistical test that measures the distance between two distributions by comparing their mean embeddings in a reproducing kernel Hilbert space—of the Koopman versus CFM generated 2D distribution density across all datasets and dynamics in Table 1., we note that MMD scores are comparable using both CFM and our Koopman approach. We also visualize the learned Koopman measurement functions in section D.1 in the Supplementary. These learned coordinates, visualized on the 2D domain, seem to reveal dataset-specific geometric patterns: radial sectors aligned with Gaussian centers in the Eight Gaussian case, and spiral patterns for the Swiss Roll. These visualizations suggest that our approach discovers fundamental geometric properties aligned with theoretical insights from dynamical systems theory, where Koopman eigenfunctions encode invariant sets and symmetries [31].

## 5.2 Scaling to Image Data

We evaluate Koopman-CFM on higher-dimensional datasets: MNIST (28×28), Fashion-MNIST (28×28), and Toronto Face Database (48×48) to assess how our linearization approach scales to realistic visual domains.

	G→2M		G→8G		G→SR		8G→G		8G→2M		8G→SR	
	OT	Gauss	OT	Gauss	OT	Gauss	OT	Gauss	OT	Gauss	OT	Gauss
Koopman MMD	0.1607	0.1090	0.0017	0.0036	<b>0.0017</b>	0.0036	<b>0.2964</b>	0.4869	0.1090	<b>0.1550</b>		0.0065
CFM MMD	<b>0.1581</b>	<b>0.1085</b>	<b>0.0012</b>	<b>0.0031</b>	0.0022	<b>0.0024</b>	0.3125	<b>0.4733</b>	<b>0.1085</b>	0.1557		<b>0.0046</b>

Table 1: MMD for 2D generative tasks across path types. Koopman-CFM achieves comparable quality scores across datasets and complexity in dynamics at a fraction of the sampling cost. Bold values represent best performance (lower the better)

**Architecture and Training.** We implement our decoder-free design as in Figure 2 using a U-Net-based convolutional encoder [38] for  $g_\theta(x)$ , concatenated with the raw image to form the composite observable. The Koopman generator  $\mathbf{L}$  operates on this representation, with training following a curriculum strategy that gradually increases trajectory length. All experiments use a pre-trained CFM model with matching architecture as the target vector field. Additional details can be found in the Supplementary Material.

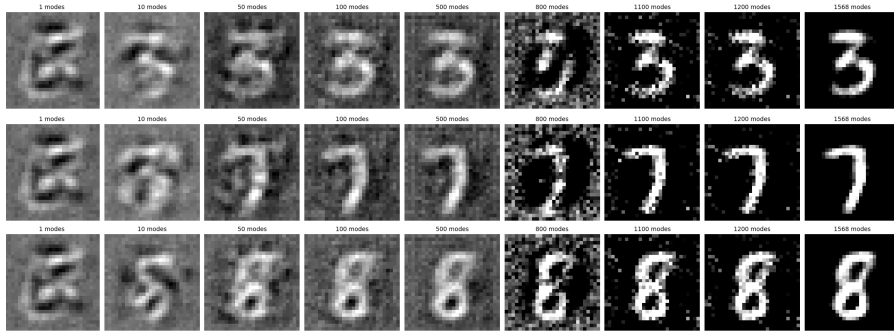


Figure 6: Progressive sample reconstructions at  $t = 1$  as Koopman modes are incrementally added (ordered by decreasing real part eigenvalue). We see that the highest modes contain the digit discerning characteristics, while the lowest most allow to create a more defined homogenous background.

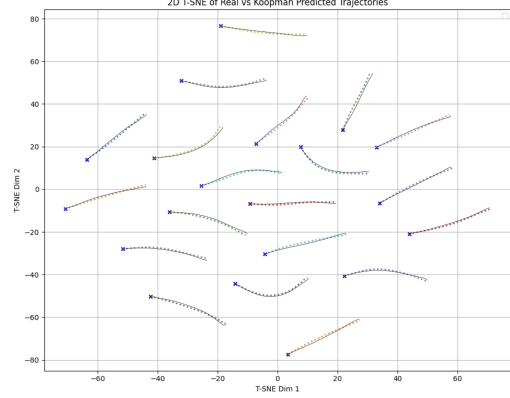
**Spectral Properties and Interpretability.** In Section D.1 in the Supplementary we describe how we can use our decoder-free Koopman approach as a means to visualize the modes of the learned Koopman operator. Spectral analysis of the learned Koopman generator reveals a structured organization of generative features. Eigenmodes with large real part eigenvalues correspond to high-frequency, class-discriminative features that evolve rapidly during generation, while those with negative real parts seem to encode slower-evolving background and global intensity patterns as can be seen when visualizing the obtained modes for MNIST, FMNIST, and TFD datasets (see Supplementary). Figure 6 shows the progressive reconstruction of MNIST digits at  $t = 1$  as we add more modes ordered from the high eigenvalue real part to low. It confirms that top modes capture essential structure while subsequent modes refine details, demonstrating how the Koopman framework naturally disentangles generative factors at different temporal scales.

**Early Semantic Emergence.** Remarkably, our Koopman embeddings exhibit strong predictive structure even when initialized from pure noise. As shown in Sections D.1 and D.2 in the Supplementary Material, projecting the embeddings onto the highest Koopman modes and visualizing them with t-SNE at  $t = 0$  reveals clear class-based clustering. This structure is absent in raw pixel space. Quantitative analysis using K-nearest neighbors confirms significantly higher class separability in Koopman space at early time points ( $t < 0.5$ ), especially under high-noise conditions ( $t < 0.2$ ). These findings not only support the idea that semantic information is encoded from the outset but also

suggest potential for controllable generation via early-stage latent manipulation. This complements our observations in Section 5.2, where we noted the emergence of meaningful structure in Koopman space even at noise-level inputs.



(a) Image sample examples from CFM and our Koopman-CFM approach

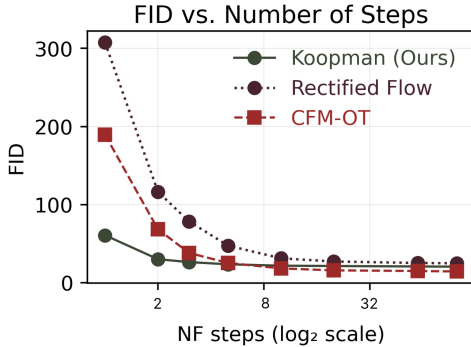


(b) t-SNE of Koopman (dashed) vs CFM (solid) trajectories on MNIST.

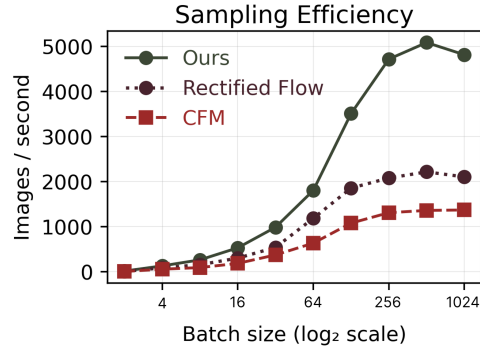
Figure 7: (a) One-shot generation samples with Koopman-CFM match CFM in quality. (b) Koopman trajectories closely follow CFM paths in latent space, confirming semantic alignment.

**Linearization Accuracy and Efficiency.** We assess the effectiveness of Koopman-CFM in capturing the true dynamics of the generative process through both qualitative and quantitative comparisons with the original CFM. As shown in Figures 7, our model produces visually coherent samples that closely match those generated by standard CFM, despite requiring only a single forward pass. Additionally, t-SNE visualizations of trajectories reveal that Koopman-predicted paths remain well-aligned with CFM trajectories even under high-dimensional, nonlinear dynamics, confirming the accuracy of our linear approximation.

Figure 8 further demonstrate that Koopman-CFM achieves competitive Fréchet Inception Distance (FID) [14] scores at dramatically reduced sampling costs, particularly excelling in the low-step regime (1–8 steps), where it outperforms existing methods, such as Rectified Flow [24] and OT-CFM, [46] in both speed and quality. These main results are further supported by additional evaluations in the supplementary material, including density evolution, trajectory alignment, FID tables, and mode-based analyses, which collectively validate the fidelity and potential interpretability of Koopman-based generation across multiple datasets and experimental settings.



(a) FID vs. sampling steps. Koopman excels at low step counts (1–8).



(b) Images/sec at matched FID. Koopman achieves faster sampling.

Figure 8: Efficiency-quality tradeoff: Left shows generative quality across sampling steps, right shows throughput. Koopman-CFM offers best performance in low-step regimes.



### 5.3 Discussion and Future Work

In this paper, we introduced a novel approach for a principled linearization of Conditional Flow Matching using Koopman Operator Theory. Our results demonstrate that Koopman-based linearization offers a promising direction for efficient and interpretable generative modeling that scales effectively to realistic image domains. Despite these promising developments, some limitations remain. For very high-resolution images, the memory requirements for storing the full Koopman generator matrix become prohibitive, and matrix exponential calculations can introduce numerical instabilities that affect generation quality. Future work could explore better network parametrization, specialized matrix exponential algorithms, or domain decomposition to address these computational challenges. Additionally, we observe that the quality gap between Koopman sampling and traditional CFM widens slightly for more complex datasets. This suggests that while linearization captures the major modes of variation, some subtle non-linear effects may still be approximated less precisely. Our training process, which fundamentally approximates solutions to differential equations, could benefit from advances in physics-informed neural networks and scientific machine learning. These techniques could enhance the fidelity of our linearization while maintaining computational efficiency. Hybrid approaches that combine Koopman predictions with lightweight refinement steps could also potentially address quality limitations in complex datasets.

### Acknowledgements

The authors would like to thank Emery Pierson and Julien Gaubil for their insightful feedback and valuable contributions throughout the course of this project.

### References

- [1] Omri Azencot, N Benjamin Erichson, Vanessa Lin, and Michael Mahoney. Forecasting sequential data using consistent koopman autoencoders. In *International Conference on Machine Learning*, pages 475–485. PMLR, 2020.
- [2] Nimrod Berman, Ilan Naiman, Moshe Eliasof, Hedi Zisling, and Omri Azencot. One-step offline distillation of diffusion-based models via koopman modeling. *arXiv preprint arXiv:2505.13358*, 2025.
- [3] Petar Bevanda, Stefan Sosnowski, and Sandra Hirche. Koopman operator dynamical models: Learning, analysis and control. *Annual Reviews in Control*, 52:197–212, 2021.
- [4] Sam Bond-Taylor, Adam Leach, Yang Long, and Chris G Willcocks. Deep generative modelling: A comparative review of vaes, gans, normalizing flows, energy-based and autoregressive models. *IEEE transactions on pattern analysis and machine intelligence*, 44(11):7327–7347, 2021.
- [5] Steven L Brunton, Marko Budišić, Eurika Kaiser, and J Nathan Kutz. Modern koopman theory for dynamical systems. *arXiv preprint arXiv:2102.12086*, 2021.
- [6] Marko Budišić, Ryan Mohr, and Igor Mezić. Applied koopmanism. *Chaos: An Interdisciplinary Journal of Nonlinear Science*, 22(4), 2012.
- [7] Hanqun Cao, Cheng Tan, Zhangyang Gao, Yilun Xu, Guangyong Chen, Pheng-Ann Heng, and Stan Z Li. A survey on generative diffusion models. *IEEE Transactions on Knowledge and Data Engineering*, 2024.
- [8] Ricky TQ Chen, Yulia Rubanova, Jesse Bettencourt, and David K Duvenaud. Neural ordinary differential equations. In *Advances in Neural Information Processing Systems (NeurIPS)*, volume 31, 2018.
- [9] Laurent Dinh, David Krueger, and Yoshua Bengio. Nice: Non-linear independent components estimation. In *Workshop on Deep Learning, NIPS*, 2014.
- [10] Laurent Dinh, Jascha Sohl-Dickstein, and Samy Bengio. Density estimation using real nvp. In *International Conference on Learning Representations (ICLR)*, 2017.
- [11] Kevin Frans, Danijar Hafner, Sergey Levine, and Pieter Abbeel. One step diffusion via shortcut models. *arXiv preprint arXiv:2410.12557*, 2024.
- [12] Margareta Grbić, Qing Li, and Ioannis G Kevrekidis. Koopman theory for generative modeling of chaotic time series. *Chaos: An Interdisciplinary Journal of Nonlinear Science*, 31(12), 2021.



- [13] Arthur Gretton, Karsten M. Borgwardt, Malte J. Rasch, Bernhard Schölkopf, and Alexander Smola. A kernel two-sample test. *Journal of Machine Learning Research*, 13(25):723–773, 2012. URL <http://jmlr.org/papers/v13/gretton12a.html>.
- [14] Martin Heusel, Hubert Ramsauer, Thomas Unterthiner, Bernhard Nessler, and Sepp Hochreiter. Gans trained by a two time-scale update rule converge to a local nash equilibrium, 2018. URL <https://arxiv.org/abs/1706.08500>.
- [15] Jonathan Ho, Ajay Jain, and Pieter Abbeel. Denoising diffusion probabilistic models. *Advances in neural information processing systems*, 33:6840–6851, 2020.
- [16] Ross Irwin, Alessandro Tibo, Jon Paul Janet, and Simon Olsson. Efficient 3d molecular generation with flow matching and scale optimal transport. In *ICML 2024 AI for Science Workshop*, 2024.
- [17] Diederik P Kingma and Prafulla Dhariwal. Glow: Generative flow with invertible 1x1 convolutions. In *Advances in Neural Information Processing Systems (NeurIPS)*, volume 31, 2018.
- [18] Stefan Klus, Feliks Nüske, Péter Koltai, Hao Wu, Ioannis Kevrekidis, Christof Schütte, and Frank Noé. Data-driven model reduction and transfer operator approximation. *Journal of Nonlinear Science*, 28: 985–1010, 2018.
- [19] Bernard O Koopman. Hamiltonian systems and transformation in hilbert space. *Proceedings of the National Academy of Sciences*, 17(5):315–318, 1931.
- [20] Bernard O Koopman and John Von Neumann. Dynamical systems of continuous spectra. In *Proceedings of the National Academy of Sciences*, volume 18, pages 255–263. National Acad Sciences, 1932.
- [21] J Nathan Kutz, Steven L Brunton, Bingni W Brunton, and Joshua L Proctor. *Dynamic mode decomposition: data-driven modeling of complex systems*. SIAM, 2016.
- [22] Yaron Lipman, Ioannis Gkioulekas, Tatsunori Hashimoto, William T Liu, Ben Poole, Ricky Richter-Powell, Robin Rombach, Ali Toker, and Jiaxin Wu. Flow matching for generative modeling. In *International Conference on Learning Representations (ICLR)*, 2023.
- [23] Enshu Liu, Xuefei Ning, Yu Wang, and Zinan Lin. Distilled decoding 1: One-step sampling of image auto-regressive models with flow matching. In *The Thirteenth International Conference on Learning Representations*, 2025.
- [24] Xingchao Liu, Chengyue Gong, and Qiang Liu. Flow straight and fast: Learning to generate and transfer data with rectified flow, 2022. URL <https://arxiv.org/abs/2209.03003>.
- [25] Xingchao Liu, Chengyue Gong, and Qiang Liu. Flow straight and fast: Learning to generate straight lines improves generalization and efficiency. In *International Conference on Learning Representations (ICLR)*, 2023. Often referred to as Rectified Flow.
- [26] Yujia Liu, Chuan Guo Li, Kuan-Chieh Zhou, and Anima Anandkumar. Flow matching with stochastic differential equations. *arXiv preprint arXiv:2306.02393*, 2023.
- [27] Simian Luo, Yiqin Wu, Surui Wang, Puchao Chen, Shijie Zhao, Jun Zhu, et al. Latent consistency models: Synthesizing high-resolution images with few-step inference. *arXiv preprint arXiv:2310.04378*, 2023.
- [28] Bethany Lusch, J Nathan Kutz, and Steven L Brunton. Deep learning for universal linear embeddings of nonlinear dynamics. *Nature communications*, 9(1):4950, 2018.
- [29] Emmanuel Menier, Sebastian Kaltenbach, Mouadh Yagoubi, Marc Schoenauer, and Petros Koumoutsakos. Interpretable learning of effective dynamics for multiscale systems. In *Proceedings A*, volume 481, page 20240167. The Royal Society, 2025.
- [30] Igor Mezić. Spectral properties of dynamical systems, model reduction and decompositions. *Nonlinear Dynamics*, 41:309–325, 2005.
- [31] Igor Mezic. Koopman operator, geometry, and learning, 2020. URL <https://arxiv.org/abs/2010.05377>.
- [32] Samuel E Otto and Clarence W Rowley. Linearly recurrent autoencoder networks for learning dynamics. *SIAM Journal on Applied Dynamical Systems*, 18(1):558–593, 2019.
- [33] Maks Ovsjanikov, Mirela Ben-Chen, Justin Solomon, Adrian Butscher, and Leonidas Guibas. Functional maps: a flexible representation of maps between shapes. *ACM Transactions on Graphics (ToG)*, 31(4): 1–11, 2012.

- [34] Adam Paszke, Sam Gross, Francisco Massa, Adam Lerer, James Bradbury, Gregory Chanan, Trevor Killeen, Zeming Lin, Natalia Gimelshein, Luca Antiga, Alban Desmaison, Andreas Köpf, Edward Yang, Zach DeVito, Martin Raison, Alykhan Tejani, Sasank Chilamkurthy, Benoit Steiner, Lu Fang, Junjie Bai, and Soumith Chintala. Pytorch: An imperative style, high-performance deep learning library, 2019. URL <https://arxiv.org/abs/1912.01703>.
- [35] F. Pedregosa, G. Varoquaux, A. Gramfort, V. Michel, B. Thirion, O. Grisel, M. Blondel, P. Prettenhofer, R. Weiss, V. Dubourg, J. Vanderplas, A. Passos, D. Cournapeau, M. Brucher, M. Perrot, and E. Duchesnay. Scikit-learn: Machine learning in Python. *Journal of Machine Learning Research*, 12:2825–2830, 2011.
- [36] Ryan Po, Wang Yifan, Vladislav Golyanik, Kfir Aberman, Jonathan T Barron, Amit Bermanto, Eric Chan, Tali Dekel, Aleksander Holynski, Angjoo Kanazawa, et al. State of the art on diffusion models for visual computing. In *Computer Graphics Forum*, volume 43, page e15063. Wiley Online Library, 2024.
- [37] Aram-Alexandre Pooladian, Alexander Gushchin, Regina Barzilay, and Tommi Jaakkola. Multisample flow matching: Straightening flows with minibatch couplings. *arXiv preprint arXiv:2305.17160*, 2023.
- [38] Olaf Ronneberger, Philipp Fischer, and Thomas Brox. U-net: Convolutional networks for biomedical image segmentation, 2015. URL <https://arxiv.org/abs/1505.04597>.
- [39] Clarence W Rowley, Igor Mezić, Shervin Bagheri, Philipp Schlatter, and Dan S Henningson. Spectral analysis of nonlinear flows. *Journal of fluid mechanics*, 641:115–127, 2009.
- [40] Yang Song and Stefano Ermon. Generative modeling by estimating gradients of the data distribution. *Advances in neural information processing systems*, 32, 2019.
- [41] Yang Song, Jascha Sohl-Dickstein, Diederik P Kingma, Abhishek Kumar, Stefano Ermon, and Ben Poole. Score-based generative modeling through stochastic differential equations. *arXiv preprint arXiv:2011.13456*, 2020.
- [42] Yang Song, Prafulla Dhariwal, Mark Zhang, and Karsten Kreis. Consistency models. In *International Conference on Machine Learning (ICML)*, 2023.
- [43] Steven H. Strogatz. *Nonlinear Dynamics and Chaos: With Applications to Physics, Biology, Chemistry and Engineering*. Westview Press, 2000.
- [44] Yoshihiko Susuki and Igor Mezić. Applied koopman operator theory for power systems technology. *Nonlinear theory and its applications, IEICE*, 7(4):430–459, 2016.
- [45] Alexander Tong, Nikolay Malkin, Guillaume Hugué, Yanlei Zhang, Jarrod Liu, Kilian Rector-Brooks, Guy Wolf, Elizabeth Creager, and Yoshua Bengio. Conditional flow matching: Simulation-free dynamic optimal transport. *arXiv preprint arXiv:2302.00482*, 2023.
- [46] Alexander Tong, Kilian FATRAS, Nikolay Malkin, Guillaume Hugué, Yanlei Zhang, Jarrod Rector-Brooks, Guy Wolf, and Yoshua Bengio. Improving and generalizing flow-based generative models with minibatch optimal transport. *Transactions on Machine Learning Research*, 2024. ISSN 2835-8856. URL <https://openreview.net/forum?id=CD9Snc73AW>. Expert Certification.
- [47] Alexander Tong et al. Torchcfm: A conditional flow matching library. <https://github.com/atong01/conditional-flow-matching>, 2023.
- [48] Ling Yang, Zhilong Zhang, Yang Song, Shenda Hong, Runsheng Xu, Yue Zhao, Wentao Zhang, Bin Cui, and Ming-Hsuan Yang. Diffusion models: A comprehensive survey of methods and applications. *ACM Computing Surveys*, 56(4):1–39, 2023.
- [49] Enoch Yeung, Soumya Kundu, and Nathan Hodas. Learning deep neural network representations for koopman operators of nonlinear dynamical systems. In *2019 American Control Conference (ACC)*, pages 4832–4839. IEEE, 2019.

## Appendix

### A Overview

The supplementary materials below provide an expanded theoretical motivation, experimental details, and additional results that support and extend the main paper. Each section corresponds to specific elements of our method and results, with backward references to the main paper for clarity.

- **Section A: Ablation Studies**

Extending Section 5.1 of the main paper, we provide ablations on loss function design, and data sampling strategies. These experiments highlight the stability, accuracy, and design benefits of our approach, particularly the effectiveness of the generator-consistency and target-alignment losses in training Koopman-CFM.

- **Section B: Additional 2D Results**

Supplementing Section 5.1 of the main paper, we provide extensive visualizations on 2D toy datasets. These include trajectory accuracy under different interpolation paths, and visualizations of measurement functions.

- **Section C: Additional Image Experiments**

Supporting Sections 5.2 and 5.3 of the main paper, we present additional qualitative and quantitative results on MNIST, Fashion-MNIST, and the Toronto Face Dataset (TFD). These include side-by-side image samples and t-SNE visualizations showing early semantic structure in Koopman embeddings. We also visualize Koopman eigenmodes and their contributions to sample reconstructions, demonstrating how spectral decomposition reveals spatio-temporal structure in the generative processes.

- **Section D: Motivation for Using the Koopman Generator and Further Mathematical Details**

This section complements the discussion in Section 4 of the main paper by motivating our focus on the continuous Koopman generator rather than the discrete operator. We explain how this choice aligns with the simulation-free nature of Conditional Flow Matching (CFM), as it provides a more direct coupling to the underlying velocity field. This section also highlights how spectral properties of the generator could enable future regularization strategies.

Together, these sections provide a deeper understanding of our Koopman-CFM framework and support its efficiency, stability, and interpretability as claimed in the main paper.

### B Ablation Studies

#### B.1 Experimental Details

We evaluate Koopman-CFM on 2D synthetic datasets including SWISS ROLL, TWO MOONS, and mixtures of Gaussians. These studies extend the design choices presented in Section 4 of the main paper, including the decoder-free structure, generator formulation, and time-augmented dynamics. These benchmarks allow us to assess the accuracy and efficiency of our method in modeling known transport dynamics under both optimal transport (OT) and Gaussian interpolation paths.

**Data Generation.** For 2D experiments, we use a custom `DynamicsDataModule` that samples input points  $(x_1, x_2, t)$  uniformly from  $[-8, 8]^2 \times [0, 1]$ . The ground-truth vector field  $v_t(x)$  is provided by a pretrained CFM model on all utilized datasets using the [47] library and is evaluated at each sampled point. To accommodate the non-autonomous nature of the dynamics, we append a constant 1 to each derivative vector, yielding  $\dot{x} = (\dot{x}_1, \dot{x}_2, 1) \in \mathbb{R}^3$ .

We discretize the time interval  $[0, 1]$  into  $N = 100$  steps and generate a total of 2 million input-target pairs, split 80/20 into training and validation sets.

In the image domain, exhaustive sampling of the high-dimensional state space is impractical due to the curse of dimensionality. Instead, we generate a large number of 100-step trajectories from Gaussian noise at  $t = 0$  to target images at  $t = 1$ , using the pretrained CFM model as a reference

flow. Our datamodule provides points along these trajectories, their corresponding time values, and evaluations of the velocity field  $v_t(x)$ . For experiments involving the consistency loss, the final target state of each trajectory is also provided. This approach assumes that trajectories capture sufficient geometric information for learning Koopman representations that generalize to unseen regions, as the flow is expected to lie on a low-dimensional manifold. Our approach builds on the CFM data setup detailed in Section 3.1 of the main paper, where the vector fields  $v_t(x)$  are obtained from a pretrained CFM model.

**Model Architecture.** In 2D settings, we use a residual MLP encoder with skip connections and SiLU activations. The encoder receives 3D input vectors  $(x_1, x_2, t)$  and produces a Koopman representation by appending learnable features to the original state variables. This representation is evolved linearly via a learned Koopman operator (a single matrix).

For image datasets, we employ a U-Net encoder [38] that takes as input the pair  $(x, t)$ , where  $x$  is an image and  $t$  is its corresponding time. The flattened U-Net output is concatenated with the flattened image and linearly evolved using the Koopman operator. Aside from this reshaping step, the procedure is identical to the 2D case.

A distinctive feature of our approach is the absence of a decoder as in [28, 1]. Instead of reconstructing the input, we extract the preserved state coordinates from the evolved Koopman features. This design removes the need for a reconstruction loss and enables direct visualization of Koopman modes. While training we have the choice of multiple loss terms:

**Koopman Generator Loss** : This loss term is the PDE that pushes the model to learn non-linear measurements that span a Koopman Generator-stable subspace in  $\mathcal{G}(\mathcal{X})$  which allows to define a finite-dimensional matrix-representation of the Koopman generator. It is local in nature.

$$\mathcal{L}_{\text{continuous}} = \mathbb{E}_{t, x_t} \|\mathbf{L}\tilde{\mathbf{g}}(x_t) - \nabla_x \tilde{\mathbf{g}}(x_t) \cdot v_t(x_t)\|^2. \quad (18)$$

**Target Consistency Loss** : Since our objective is to obtain accurate samples from long-range evolution under the Koopman generator, we propose the following loss, which ensures consistency between the Koopman evolution and the target sample.

$$\mathcal{L}_{\text{target}} = \mathbb{E}_{t_i, x_{t_i}} \left\| e^{\mathbf{L}(1-t_i)} \begin{bmatrix} x_{t_i} \\ g_\theta(x_{t_i}) \end{bmatrix} - \begin{bmatrix} x_1 \\ g_\theta(x_1) \end{bmatrix} \right\|^2. \quad (19)$$

**Prediction loss:** We also have the option of employing this additional loss term.

$$\mathcal{L}_{\text{prediction}} = \mathbb{E}_{t, x_t} \|\text{Proj}(\mathbf{Lg}(x_t)) - v_t(x_t)\|^2. \quad (20)$$

The various gradient terms are obtained via Pytorch’s automatic-differentiation function and the  $v_t$  vector fields are pretrained using the TorchCFM library [34, 46, 45].

**Training Details.** The encoder and Koopman operator are trained jointly using the algorithm 1 . The Adam optimizer is employed for both the operator and encoder with separate learning rates:

- **Encoder learning rate:** 0.001
- **Koopman operator learning rate:** 0.0001

A specific consideration in training the Koopman model on image datasets (which employ the consistency loss) is the strategy used to sample states along the trajectories. Since our method relies on learning a linear time-evolution operator in a lifted space, the temporal distribution of training samples can significantly impact the model’s ability to generalize across time.

We compare three sampling strategies: (i) sampling states with linearly increasing time from  $t = 0$  to  $t = 1$ , (ii) sampling in reverse from  $t = 1$  to  $t = 0$ , and (iii) randomly sampling timepoints along the trajectory. These strategies are evaluated to assess the effect of temporal bias and coverage on the learned Koopman representation. The motivation stems from our intuition that learning for  $t = 1$  to  $t = 0$  allows the model to train on an increasingly difficult problem (longer time range predictions) and the observation that early-time observations often contain sufficient structure to extrapolate to  $t = 1$  via the Koopman operator.

All experiments are conducted on a single NVIDIA RTX3090 GPU, with early stopping based on validation performance. Additional architectural and hyperparameter details are provided in Table 2.

	MNIST	Fashion-MNIST	TFD
Dynamics training steps	20k	25k	5k
Number of trajectories	20k	20k	10k
Channels	32	32	64
Depth	1	1	2
Channels multiple	1,2,2	1,2,2	1,2,2
Heads	1	1	4
Head channels	-1	-1	64
Attention resolution	14,7	14,7	14,7
Dropout	0	0	0.1
Batch size	64	256	124
Epochs	8	8	12
Scheduler	ReduceLROnPlateau	ReduceLROnPlateau	ReduceLROnPlateau
Warmup steps	10	10	10
Encoder learning rate	$1 \times 10^{-3}$	$1 \times 10^{-3}$	$1 \times 10^{-3}$
Operator learning rate	$1 \times 10^{-4}$	$1 \times 10^{-4}$	$1 \times 10^{-4}$
Initial operator std	0.001	0.001	0.0005
Operator weight decay	0.0	0.0	0.01

Table 2: Grouped hyperparameters for Koopman-CFM training on MNIST, Fashion-MNIST and Toronto Faces.

## B.2 Encoder-Decoder vs Decoder-Free Architectures

The encoder-decoder setup, despite identical training to the decoder-free parametrization showcased in 4.2, leads to notable mismatches, with the Koopman and CFM trajectories diverging as seen in Figure 9. This demonstrates that removing the decoder not only reduces model complexity but also enhances the faithfulness of the learned Koopman dynamics, improving alignment and sampling accuracy across the full time-domain and dynamic complexity (Figure 10).

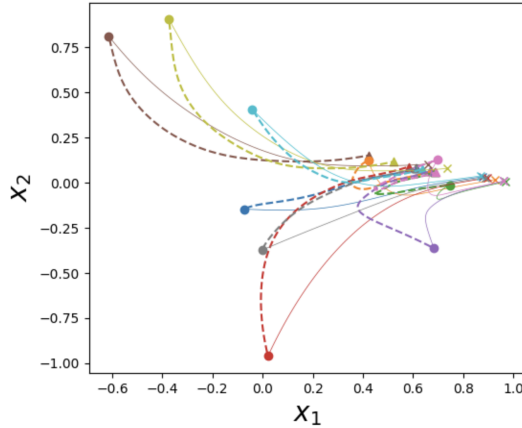


Figure 9: Trajectory comparison for Koopman-CFM using encoder-decoder between CFM trajectories (solid lines) and Koopman predicted rollouts (dashed lines). Despite the simplicity of the setting (2D problem and OT-CFM), the encoder-decoder model fails to produce accurate trajectories in the time-dependent setting.

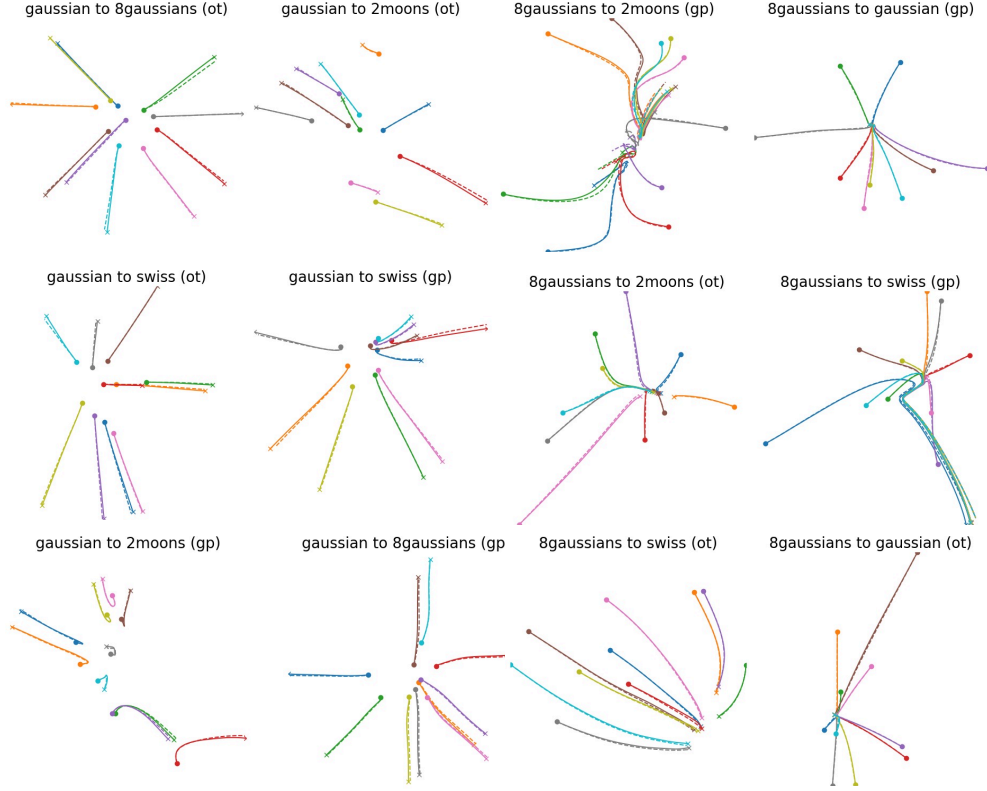


Figure 10: Trajectory comparisons between CFM and Koopman-CFM across 2D datasets using Gaussian and OT interpolation paths. The Koopman-predicted rollouts (dashed lines) align closely with CFM dynamics (solid lines), and we see that our method correctly incorporates the time dependency throughout the temporal domain regardless of path curvature.

### B.3 Influence of the different Loss Terms

Table 3 presents an ablation study on MNIST evaluating the impact of different loss terms using the Fréchet Inception Distance (FID) as the evaluation metric. We compare models trained with: (i) only the generator loss and (ii) generator and consistency loss.

The results show that using both loss terms yields the lowest FID scores, indicating the highest sample quality. The generator loss is essential for locally faithful Koopman dynamics, while the target-consistency loss promotes global temporal coherence. Their combination enables higher-fidelity generation.

Table 3: Loss ablation performed on the MNIST dataset

	$\mathcal{L}_{\text{generator}}$	$\mathcal{L}_{\text{generator+consistency}}$
FID	38	20

## C 2D Datasets

### C.1 Additional Qualitative Illustrations

We present additional qualitative results to support our choices and display the effectiveness of Koopman-CFM on 2D datasets. These visual results complement the experiments in Section 5.1 of the main paper, where Koopman-CFM was shown to closely approximate CFM trajectories on toy datasets. These visualizations demonstrate the ability of our method to approximate complex time-dependent non-linear dynamics with a linear operator in a lifted space.

#### Distribution Evolution

In Figure 11, we visualize the evolution of the generated data distribution over time under CFM and Koopman-CFM. Despite relying on a single matrix exponential, Koopman-CFM closely matches the density flow produced by the original time-integrated CFM model and achieves this at a fraction of the sampling time (see Table 1 in main paper).

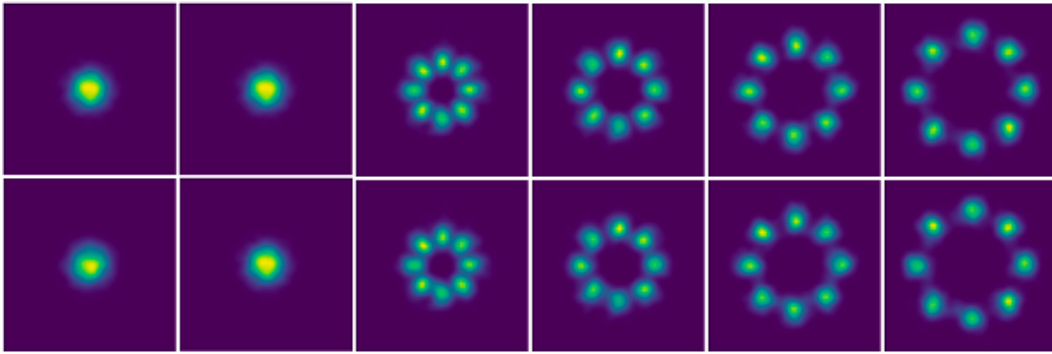


Figure 11: Evolution of generated data density when generating 8 Gaussians (8G) from the unit Gaussian prior (G) over time ( $t = 0.25$  to  $t = 1.0$ ) under CFM (top) vs. Koopman-based one-step sampling (bottom). Koopman dynamics approximate the full evolution through a single matrix exponentiation, avoiding expensive ODE integration.

#### Measurement Function Visualization

Figure 12 provides insight into the learned Koopman measurement functions. On the left, we show the OT field with trajectories. On the right, the learned observables — i.e., the non-linear measurement functions  $g_i$  — form a foliation-like structure over the input domain, highlighting how the encoder organizes the space to enable linear evolution in the Koopman representation. These qualitative results collectively demonstrate that Koopman-CFM accurately captures transport geometry, respects time-evolution structure, and yields interpretable features even in low-dimensional settings.

### C.2 Additional Quantitative Results: MMD Metric and Sampling Speed

## D Image Datasets

We extend our evaluation of Koopman-CFM to high-dimensional generative tasks using MNIST, Fashion-MNIST, and the Toronto Face Dataset (TFD). These experiments assess the method’s scalability, sampling efficiency, and interpretability when modeling complex image distributions. These results support Sections 5.2 and 5.3 of the main paper, where we discussed Koopman-CFM’s performance on image datasets and highlighted its spectral interpretability.

### D.1 Additional qualitative results

**Sampling Accuracy and Trajectory Fidelity.** To evaluate Koopman-CFM’s effectiveness in the image domain, we assess both *one-shot sampling quality* and *multi-step rollout fidelity*:

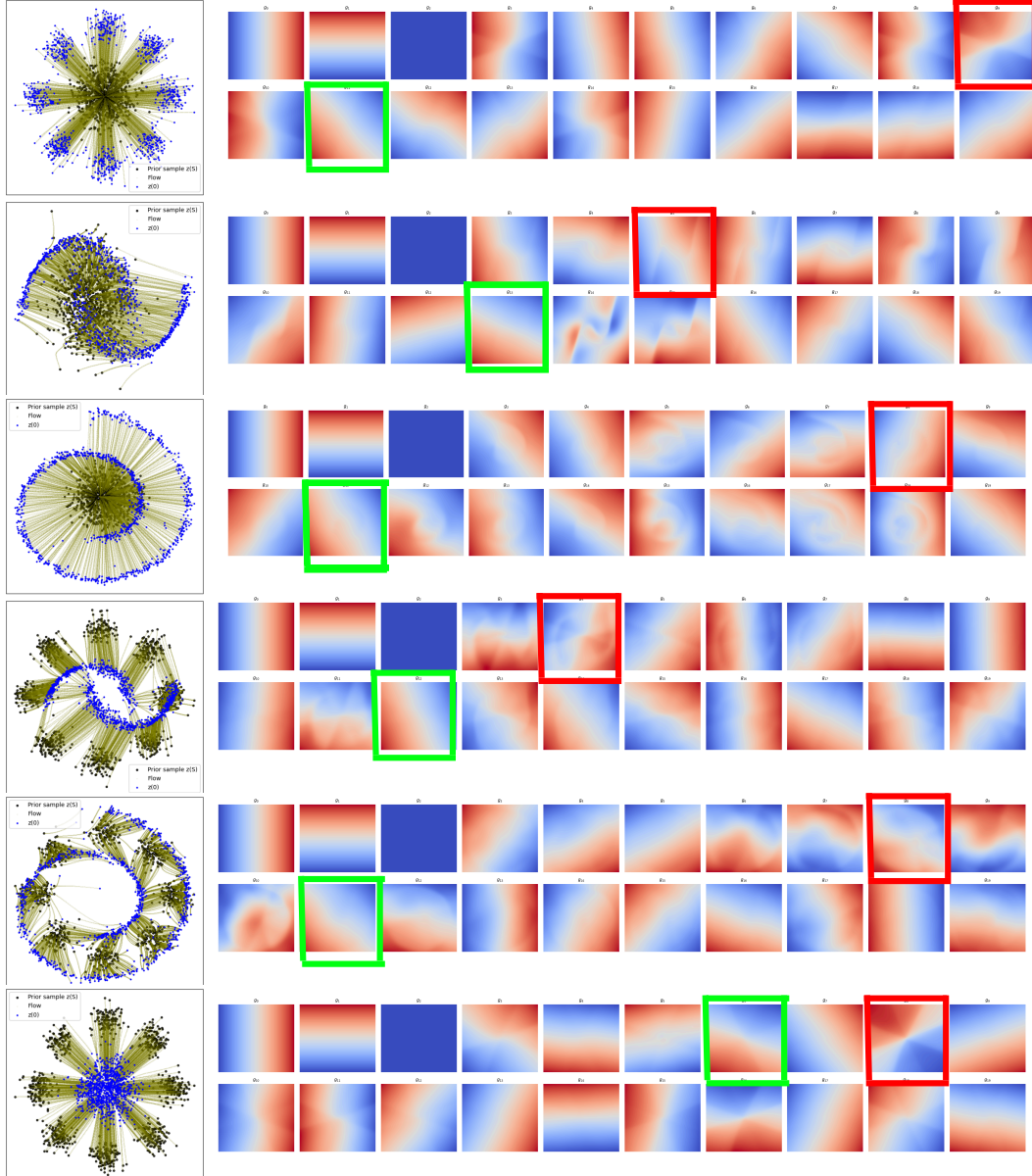


Figure 12: Left: Vector field and trajectories for an OT path from 8-Gaussian prior to target. Right: Koopman measurement functions — i.e., the non-linear functions  $g_i$  constituting the encoded vector  $[x, g_1(x), \dots, g_i(x), \dots]^\top$ . These measurement functions reveal characteristic spatial structure, with foliation patterns aligned to domain geometry (red boxes). Commonalities across priors and dynamics are highlighted (green boxes).



- **One-shot sampling** is performed using Algorithm 2 in the main paper with  $t = 1$ , enabling direct generation through matrix exponentiation.
- **Trajectory fidelity** is evaluated by comparing intermediate predictions from Koopman-CFM to full rollouts from the pretrained CFM model.

As shown in Figures 7 in the main paper, Koopman-CFM produces visually coherent samples and accurately follows complex generative paths. While one-shot FID [14] scores higher than those of multi-step CFM, the overall trajectory quality after T-SNE dimensionality reduction remains consistent across the full time horizon as seen in Figure 7(b) in the main paper and underlines the potential for such an approach to achieve competitive sampling in both quality of samples and efficiency.

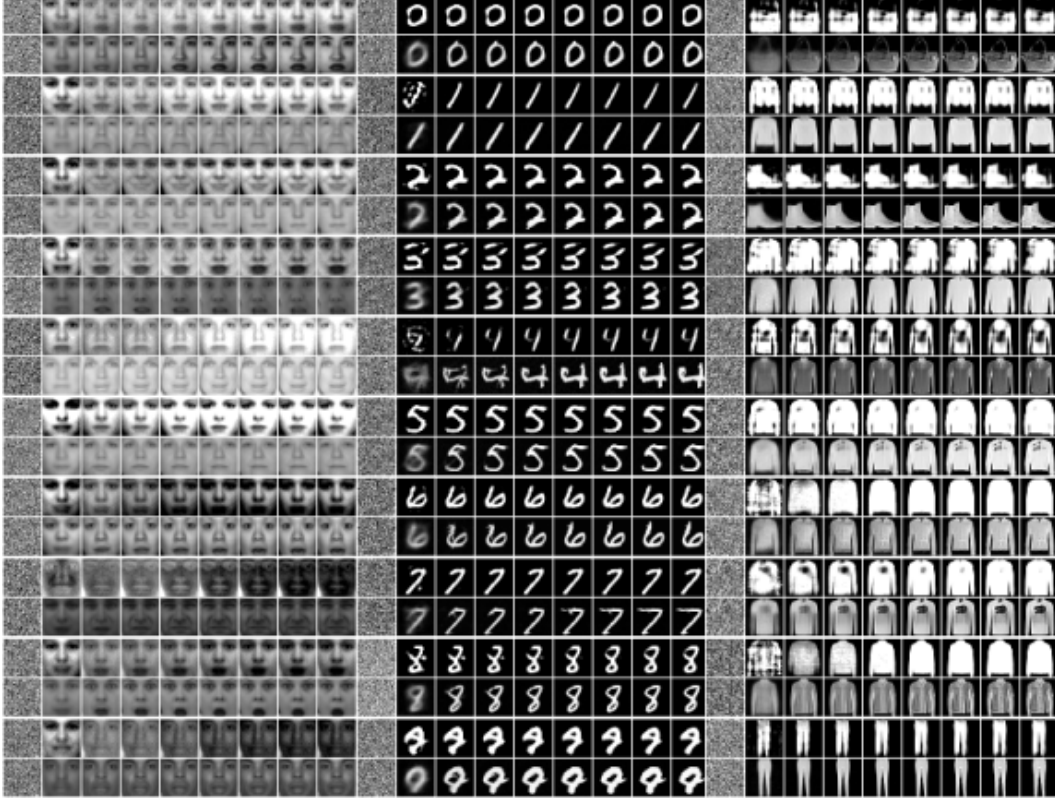


Figure 13: Visual comparison of samples generated by Koopman-CFM (bottom) and CFM (top) from identical Gaussian initializations. Koopman-CFM yields visually coherent results with dramatically faster sampling.

**Spectral Structure and Koopman Modes.** As mentioned in Section 4.4, a distinctive advantage of our decoder-free Koopman formulation, compared to standard encoder-decoder architectures [28, 1], is that it enables direct visualization of the learned eigenmodes, offering insight into the modal composition of the generative process [5, 31]. Because the Koopman generator is applied to an augmented state  $\tilde{\mathbf{g}}_i = [x_i, g_i]^\top$ —where  $x_i$  is the original state and  $g_i$  is the learned observable—we can analyze its spectral decomposition directly:

$$\mathbf{L}\tilde{\mathbf{g}}_i = \lambda_i\tilde{\mathbf{g}}_i = \lambda_i \begin{bmatrix} x_i \\ g_i \end{bmatrix}. \quad (21)$$

This allows us to interpret  $x_i$ , the state part of each eigenvector, as a spatio-temporal coherent structure in image space. Since our Koopman model accurately predicts CFM trajectories across the full timespan, these modes provide a meaningful breakdown of how semantic features evolve over time. Indeed, the eigenvalue–eigenvector pairs allow us to decompose the encoded noisy sample

throughout generation via:

$$g(x_t, t) = \sum_i \alpha_i e^{\lambda_i t} \tilde{g}_i, \quad (22)$$

where  $\alpha_i$  are coefficients projecting the initial encoded gaussian noisy onto the Koopman eigenbasis. This decomposition generalizes the Fourier transform to non-linear systems. Unlike Fourier modes, which are not invariant under non-linear dynamics, Koopman modes evolve independently under the generator. Similar to Fourier analysis, this provides rich information about the underlying CFM dynamics. The real part of each eigenvalue governs amplification or decay, while the imaginary part encodes oscillations. These modes highlight spatially coherent structures in image space from which the image datasets are composed. As highlighted in Section 4.4 of the main paper, this modal decomposition provides insight into temporal scaling and spatial coherence in the generative process.

To further illustrate the sort of information contained in this spectral decomposition, we visualise in Figure 16 a subset of the learned modes, ordered by the magnitude of their corresponding eigenvalue real part, from our observations it seems:

- **Low-frequency modes** low frequency image components, such as homogeneous backgrounds on MNIST.
- **Mid-frequency modes** refine spatial structure and contour.
- **High-frequency modes** add higher frequency detail that allows to discern the class of the samples such as strokes in MNIST, facial features in TFD.

Figure 6 in the main paper, suggests that all the modes are necessary to provide accurate samples. Indeed as we progressively feed the modes (from high real part to low), we observe that the high modes allow generation of digit-discerning features, whilst the lower modes allow for a cleaner background (this is in line with what the visualized modes suggest in Figure 14).

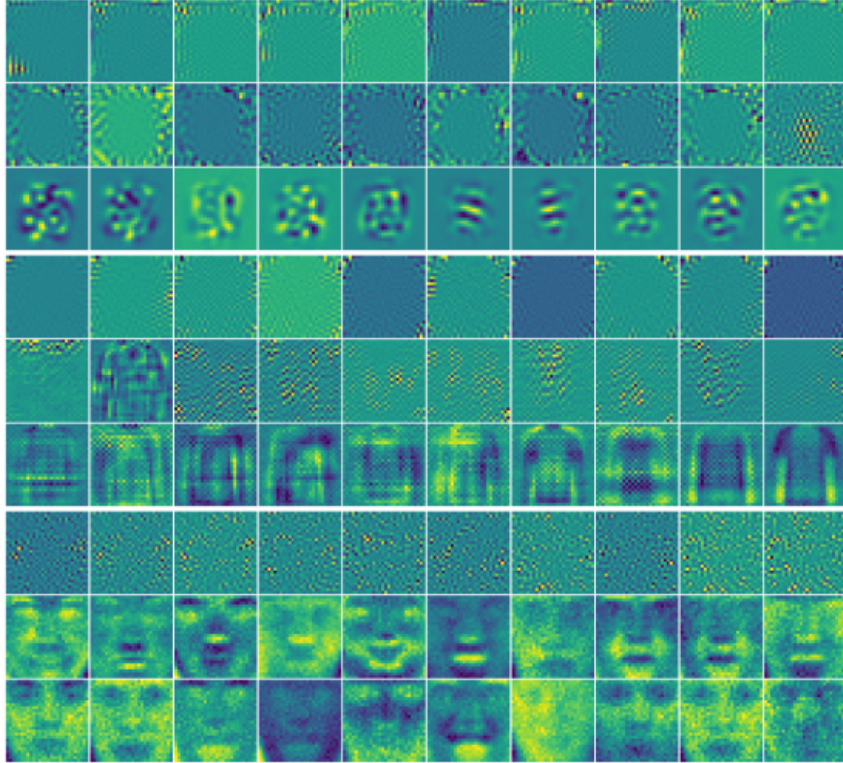


Figure 14: Visualization of learned Koopman eigenmodes for MNIST (top block), F-MNIST (middle block) and TFD (bottom block). Top: low-frequency modes; Middle: mid-frequency modes; Bottom: high-frequency modes. Each set captures distinct generative structures corresponding to different temporal scales (ie:  $\mathcal{R}(\lambda)$ ).

**Emergent Semantics in Early Embeddings.** We further probe the information content of these spectral features by projecting the encoded images, at all noise levels between  $t = 0$  to  $t = 1$  onto

subsets of modes (low, middle and high modes). In Figure 15, we project noisy Koopman encodings onto a subset of the Koopman modes across time and perform dimensionality reduction via t-SNE and label according to digit labels (we do the same with the raw pixel representation). Koopman embeddings exhibit class-separated clusters much earlier in the generation process, suggesting that the learned representation captures semantically aligned directions at all noise levels. This is quantitatively supported in Figure 17, where KNN classification accuracy in Koopman space outperforms pixel space especially in the highly noisy regimes. The analysis also suggest that the label discriminative information is contained in the high modes.

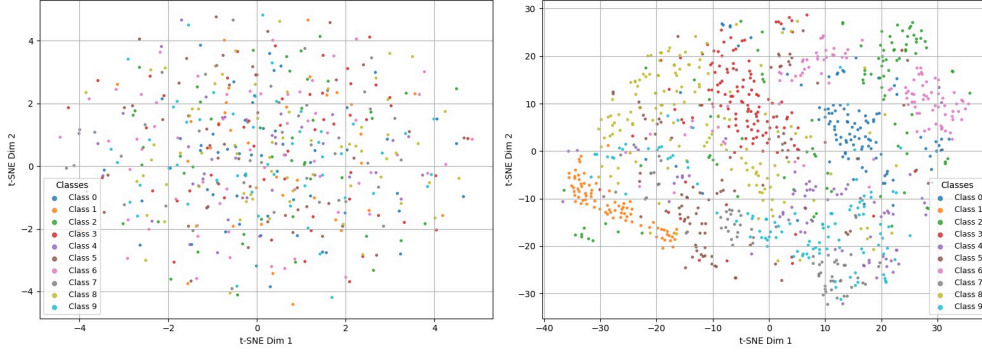


Figure 15: t-SNE plots comparing Koopman embeddings projected on the subset of modes with high real eigenvalue part against those of the raw pixel space at  $t = 0$  corresponding to the pure noise setting. Koopman embeddings exhibit greater class separation and predictive structure even.

**Operator Structure.** Finally, we visualize the learned Koopman generator matrix throughout training in Figure 16. In light of our Koopman encoder parametrisation:  $[x, g(x)]^T$ , our operator can be viewed in a block structured form:

$$L = \begin{bmatrix} L_{xx} & L_{gx} \\ L_{xg} & L_{gg} \end{bmatrix}$$

where:

- $L_{xx}$  captures linear interactions within the state variables,
- $L_{xg}$  encodes how the state drives non-linear measurements,
- $L_{gx}$  represents how non-linear features influence the state,
- $L_{gg}$  governs the dynamics among the non-linear features themselves.

During training, as seen in Figure 16, we observe emergent block structure and sparsity patterns. Pixels seem to interact mostly with their neighboring pixel measurements (whether linear or non-linear), likely due to the inductive biases of the convolutional encoder. Over the course of training, we notice that the blocks characterizing non-linear interactions strengthen, suggesting that the model is progressively capturing the underlying non-linear dynamics. This behavior is consistent across the image datasets and reflects the localized inductive biases encoded in our convolutional architecture (see Section 4.2, main paper).



Figure 16: Training evolution (arrow indicates longer training) of the Koopman operator. Block-sparse structures emerge, reflecting localized dependencies among observables.

## D.2 Additional Quantitative Evaluations

To further assess the performance of Koopman-CFM in the image domain, we complement the qualitative results from Section D.1 with a set of quantitative benchmarks evaluating both generative quality and sampling efficiency. These results support the findings discussed in Sections 5.2 and 5.3 of the main paper.

**FID Scores Across Datasets.** In Table 4, we report Fréchet Inception Distance (FID) scores for Koopman-CFM and baseline CFM models across MNIST, Fashion-MNIST (FMNIST), and the Toronto Face Dataset (TFD). Each method is evaluated under both one-step sampling and full 100-step rollouts. While multi-step CFM achieves lower FID on more complex datasets, Koopman-CFM remains competitive, especially on MNIST, and provides added interpretability through spectral insights.

**Embedding-Level Class Separability.** Finally, Figure 17 explores the semantic structure of Koopman embeddings by measuring K-nearest neighbor (KNN) classification accuracy over time. Compared to raw pixel features, Koopman projections—especially onto high-frequency modes—show higher class separability even at early time steps ( $t \leq 0.3$ ). This validates our claims (Sections 4.4 and 5.3, main paper) regarding the interpretability and semantic alignment of our learned embedding space, indeed digit class is discernible even in highly noisy regimes.

Method / FID Score	MNIST	FMNIST	TFD
Koopman (1-step)	60.6	188	138
CFM (1-step)	190	150	53.3
Koopman (100-steps)	20.2	146.2	130
CFM (100-steps)	14	16.1	21.4

Table 4: FID scores and sampling times for Koopman-CFM and baselines across image datasets. As dataset complexity increases, the FID gap between Koopman-CFM and traditional CFM increases. We believe this can be improved, but the Koopman approach offers valuable insights via spectral analysis.

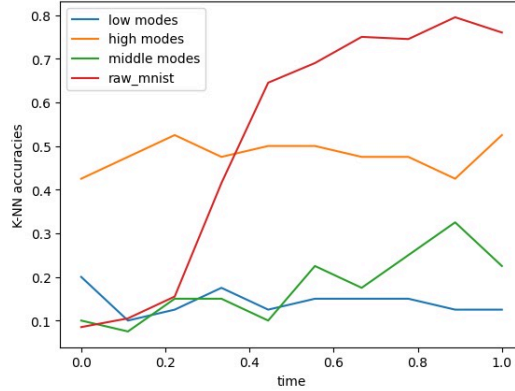


Figure 17: Left: t-SNE clustering of Koopman embeddings at  $t = 0$  projected onto the top 50 Koopman modes, showing class separation. Right: KNN classification accuracy on raw pixels vs. projections on high/mid/low Koopman modes over time. Koopman embeddings yield stronger class separation earlier.

## E Motivation for Using the Koopman Generator

As discussed in the main text, there are two principal approaches for learning Koopman representations: learning the discrete Koopman operator or the continuous Koopman generator. In this section, we provide additional motivation for focusing on the generator, particularly in light of future applications involving flow regularization.

As discussed in Section 3.1 of the main paper, Conditional Flow Matching (CFM) defines a simulation-free objective that learns the velocity field  $v_t(x)$ . Here, we expand on this formulation by exploring the non-uniqueness of these vector fields and motivating the Koopman generator as a regularized representation.

### E.1 Non-Uniqueness of CFM Vector Fields

As introduced in Section 3.1 of the main paper, CFM learns a time-dependent velocity field  $v_t(x)$  that pushes forward a prior distribution to a target distribution, without requiring access to full trajectories. The transformation is defined by the ODE:

$$\frac{dx_t}{dt} = v_t(x_t). \quad (23)$$

For a fixed vector field, this ODE has a unique solution for each initial condition. However, for a given pair of prior and target distributions, there are infinitely many vector fields that satisfy the transport condition. Recent works (e.g., Rectified Flows [25], OT-CFM [46]) address this by regularizing the learned dynamics to prefer straight or minimal-action trajectories, which also helps in reducing numerical integration costs.

We note that this observation and the associated techniques align very well with our framework and motivates the future use of Koopman-based representations as a vehicle *for regularization*. In this work, we do not apply any explicit regularization to the flow; instead, we assess whether it is feasible to learn an accurate Koopman generator given a fixed, pretrained vector field  $v_t(x)$ . Our emphasis on the Lie generator (rather than the Koopman operator itself) also stems from its direct alignment with this goal.

### E.2 Motivation for the Koopman Generator in light of potential CFM Flow-regularization

This complements Section 3.2 of the main paper, where we introduced the Koopman generator  $\mathcal{L}$  and discussed its alignment with CFM’s differential formulation. The following comparison provides further justification for its use in our setting.

**Discrete Case: Koopman Operator.** The discrete Koopman operator evolves a function  $g$  over a finite time step  $\Delta t$ :

$$K_{\Delta t}g(x_t) := g \circ F_{\Delta t}(x_t),$$

where  $F_{\Delta t}(x_t)$  is the flow map defined via the integral of  $v_t$ . Learning this operator typically involves minimizing:

$$\mathcal{L}_{\text{discrete}} = \mathbb{E}_{t, x_t, x_{t+\Delta t}} \|\mathbf{K}\mathbf{g}(x_t) - \mathbf{g}(x_{t+\Delta t})\|^2. \quad (24)$$

This requires access to both  $x_t$  and  $x_{t+\Delta t}$ , and implies a dependency on discretized trajectory segments.

**Continuous Case: Koopman Generator.** In contrast, the continuous Koopman generator relates the temporal derivative of  $g$  to the velocity field:

$$\mathcal{L}g(x_t) := \frac{d}{dt}g(x_t) = \nabla_x g(x_t) \cdot v_t(x_t),$$

with a corresponding learning objective:

$$\mathcal{L}_{\text{continuous}} = \mathbb{E}_{t, x_t} \|\mathbf{L}\mathbf{g}(x_t) - \nabla_x \mathbf{g}(x_t) \cdot v_t(x_t)\|^2. \quad (25)$$

This complements the continuous Koopman generator formulation in Section 3.2 of the main paper, providing further insight into its alignment with local flow field learning. This formulation avoids explicit time integration and instead focuses on local derivatives evaluated at the same point  $x_t$ . It aligns more closely with the differential, simulation-free structure of CFM. Although we do not apply regularization in this work, the continuous Koopman generator is a natural object for future efforts in that direction. The Koopman literature [5, 12, 3, 20] suggests that spectral and structural properties of the generator (e.g., skew-symmetry, normality) can reflect physical constraints such as conservation or reversibility. For instance, in Hamiltonian systems, the scalar Hamiltonian function  $\mathcal{H}(p, q)$  is a Koopman eigenfunction with eigenvalue zero:

$$\frac{d\mathcal{H}(p, q)}{dt} = \frac{\partial \mathcal{H}}{\partial q} \frac{\partial q}{\partial t} + \frac{\partial \mathcal{H}}{\partial p} \frac{\partial p}{\partial t} = \frac{\partial \mathcal{H}}{\partial q} \frac{\partial \mathcal{H}}{\partial p} - \frac{\partial \mathcal{H}}{\partial p} \frac{\partial \mathcal{H}}{\partial q} = 0. \quad (26)$$

In such systems, the Koopman operator is unitary, and the generator is skew-symmetric. These structural properties can, in principle, be used as inductive biases or constraints in future training pipelines.

Our focus in this paper is on assessing the feasibility of learning the Koopman generator with a fixed pretrained vector field. However, our broader motivation for favoring the generator over the operator is its tighter coupling to the local dynamics, which could enable more principled and physically meaningful regularization strategies in future joint CFM flow and Koopman representations training setups.